

Numerical simulations of large deformation of thin shell structures using meshfree methods

S. Li, W. Hao, W. K. Liu

102

Abstract In this paper, meshfree simulations of large deformation of thin shell structures is presented. It has been shown that the window function based meshfree interpolants can be used to construct highly smoothed (high order “manifold”) shape functions for three-dimensional (3-D) meshfree discretization/interpolation, which can be used to simulate large deformation of thin shell structures while avoiding ill-conditioning as well as stiffening in numerical computations.

The main advantage of such 3-D meshfree continuum approach is its simplicity in both formulation and implementation as compared to shell theory approach, or degenerated continuum approach. Moreover, it is believed that the accuracy of the computation may increase because of using 3-D exact formulation. Possible mechanism to relieve shear/volumetric locking due to the meshfree interpolation is discussed. Several examples have been computed by using a meshfree, explicit, total Lagrangian formulation. Towards to developing a self-contact algorithm, a novel meshfree contact algorithm is proposed in the end.

1 Introduction

The numerical simulation of linear/non-linear thin shell structures has been a challenge in applied mechanics and in many engineering branches. Its engineering significance as well as technical difficulties can be best measured by the seemingly ever-lasting “new formulations” or “new contributions” in the literature throughout the century, not mentioning the early contributions. Its applications cover from almost every aspects of engineering, for instance, sheet metal forming, crash-worthiness test, civil structure design, pressure vessel liability, shipbuilding, just to name a few.

Regarding the strategy of numerical simulations of thin shell structures, there are three major approaches: (a) numerical simulation based on linear/nonlinear shell theories; (b) so-called degenerated continuum, or continuum based approach; (c) direct three-dimensional (3-D) continuum approach.

Among these three approaches, 3-D continuum direct approach is the simplest, and most accurate one in principle; nonetheless it is the least popular one in practice, though it has not been completely abandoned; the multiple-quadrature hexahedral element proposed by Liu et al. [22] and Liu et al. [21] is a representative of it. However, such ad-hoc 3-D continuum element is usually very complicated in design in order to avoid all possible pathological scenarios. The major setback, or dilemma that prevents using lower order finite element in 3-D direct simulation is that it is often required to deploy multiple elements in the thickness direction of the thin shell to acquire reasonable gradient field, which, on the other hand, leads to degrading the conditioning of the discrete system and then the accuracy of the numerical solution; moreover, the direct continuum approach is very expensive, which usually requires more elements (3 to 5 times) in the same simulation than shell theory approach, or degenerated approach does.

It seems to us that the most commonly used numerical algorithms belong to the so-called degenerated continuum approach (e.g. Hughes and Liu [12, 13], Stanley [31]). Compared to shell theory approach, the degenerated approach is much simpler; however, for nonlinear large deformation of inelastic shells, its formulations are still very much involved. The main reason for this is because some degenerated continuum elements suffer from shear locking as well as membrane locking (Stolarski and Belytschko [32]). To avoid such numerical pathologies, using sophisticated mixed formulations, such as “enhanced strain” formulation, or other incompatible element approaches, is inevitable. Moreover, it is troublesome, if it is not impossible, to embed complicated constitutive laws into the degenerated continuum formulation, such as the thermo-elasto-viscoplasticity with damage at finite strain.

There have been some works on using meshfree methods to simulate large deformation of solids, e.g. Chen et al. [6, 5]; nonetheless, to the authors’ knowledge, there has not been any successful attempts reported in literature dealing with nonlinear large deformation of thin shell structures via meshfree methods. In this study, we attempt to use window function based meshfree interpolants to directly simulate large deformation of thin shell/sheet

S. Li, W. Hao, W. K. Liu (✉)
Department of Mechanical Engineering,
Northwestern University, 2145 Sheridan Road, Evanston,
IL 60208, USA

This work is supported by grants from the the Army Research Office, and National Science Foundations. It is also sponsored in part by the Army High Performance Computing Research Center under the auspices of the Department of the Army, Army Research Laboratory cooperative agreement number DAAH04-95-2-003/contract number DAAH04-95-C-0008, the content of which does not necessarily reflect the position or the policy of the government, and no official endorsement should be inferred.

structures as what they really are – three dimensional solid. By doing so, we can enjoy both the simplicity in formulation as well as the improvement in accuracy. The novelty, more precisely, the advantage of such meshfree approach are: (a) the ability to alleviate both volumetric locking as well as shear locking; (b) the ability to alleviate ill conditioning due to small thickness and large aspect ratio; (c) the ability to capture gradient field in thickness direction with relative small number of particles in thickness direction (2 or at most 3). Lacking these abilities might be the reason why 3-D direct simulation have been inhibitive for finite element methods.

So far, we have not been able to understand completely why window based meshfree interpolants have such amiable properties. The justification and rational for it are: first the window function based meshfree methods are a class of “high order manifold” discretizations, meaning that the discretization field is highly smooth, more than $C^3(\Omega)$ in general; This highly smooth discretization may do some good in computations, because of its obvious tendency to alleviate ill condition number caused by the length scale of the smallest dimension. Furthermore, the “high order manifold” meshfree methods used here is a discretization that one can increase the smoothness of the discretization without increasing the degrees of freedoms, or total number of particles of the whole system, which is almost impossible to do using finite element type interpolation. This unique property may be why, at least we suspect so, certain higher order reduced integration strategies are available, which could reduce “locking” while avoid rank deficiencies at the same time. Second, the relative large support size of the meshfree shape function will delay the “mesh” distortion significantly in large deformation computation, thus such meshfree computations can sustain “extremely” large deformation without recourse to any “remesh” or particle relocation, compared to finite element approaches.

It may be true that part of these special traits may be also shared by higher order finite element too; however, for finite element method to construct higher order element in a 3-D thin shell structure may require more nodal points distributed along thickness direction, which will lead to bad conditioning of the algebraic system; this might be the reason that such computational practice has rarely been performed and reported in the literature.

The paper is organized in following order: in Sect. 2 some of the basic technique ingredients of meshfree methods are outlined, and the emphasis is placed on 3-D formulation; then the proposed meshfree discretization/ formulation is tested for three different materials: (1) elasto-viscoplastic material (Sect. 3), (2) hyperelastic material (Sect. 4), and (3) a J_2 elasto-plastic material (Sect. 5). A brief discussion of a new meshfree contact algorithm is carried out in Sect. 6.

2

Basic ingredients of the technique

First, a brief review of reproducing kernel particle method and the corresponding Galerkin formulation in the context of 3-D large deformation is outlined.

2.1

3-D reproducing kernel particle shape function

For general formulation of meshfree methods, readers are referred to the comprehensive review by Belytschko et al. [4], or Liu et al. [19]. For the latest development in meshfree method, we mention the work of Atluri and Zhu [1, 2, 34].

As one of meshfree methods, the reproducing kernel particle method (RKPM) is systematically formulated in Liu et al. [23, 20, 24], Li and Liu [16, 17]. The 3-D tri-linear RKPM meshfree shape function used in computations is constructed by using following polynomial basis,

$$\mathbf{P}(X) = \{1, X_1, X_2, X_3, X_1X_2, X_2X_3, X_3X_1, X_1X_2X_3\}, \quad (1)$$

where $X := (X_1, X_2, X_3)$. Embedding either a cubic spline box function, or a fifth order spline box function as window function, the kernel function can be explicitly written as,

$$\mathcal{H}_\ell(X) := \mathbf{P}\left(\frac{X_\ell - X}{\rho}\right) \mathbf{b}(X) \phi_\rho(X_\ell - X) \Delta V_\ell \quad (2)$$

where $\mathbf{P}(X)$ is the polynomial basis, $\phi_\rho(X)$ is the normalized window function, ΔV_ℓ is the integration weight, and the vector $\mathbf{b}(X)$ is determined by solving the following algebraic equation,

$$\mathbf{M}(X)\mathbf{b}(X) = \mathbf{P}(0), \quad \text{and} \quad \mathbf{P}(0) = \{1, 0, \dots, \dots, 0, 0, 0\}^T \quad (3)$$

where both moment matrix, \mathbf{M} , and \mathbf{b} vector are functions of X ; thus Eq. (3) has to be solved at each Gauss quadrature point. In detail, one can write Eq. (3) as

$$\begin{pmatrix} m_{000}^h & m_{100}^h & m_{010}^h & m_{001}^h & m_{110}^h & m_{011}^h & m_{101}^h & m_{111}^h \\ m_{100}^h & m_{200}^h & m_{110}^h & m_{101}^h & m_{210}^h & m_{111}^h & m_{201}^h & m_{211}^h \\ m_{010}^h & m_{110}^h & m_{020}^h & m_{011}^h & m_{120}^h & m_{021}^h & m_{111}^h & m_{121}^h \\ m_{001}^h & m_{011}^h & m_{011}^h & m_{002}^h & m_{111}^h & m_{012}^h & m_{102}^h & m_{112}^h \\ m_{110}^h & m_{210}^h & m_{120}^h & m_{111}^h & m_{220}^h & m_{121}^h & m_{211}^h & m_{221}^h \\ m_{011}^h & m_{111}^h & m_{021}^h & m_{012}^h & m_{121}^h & m_{022}^h & m_{112}^h & m_{122}^h \\ m_{101}^h & m_{201}^h & m_{111}^h & m_{102}^h & m_{211}^h & m_{112}^h & m_{202}^h & m_{212}^h \\ m_{111}^h & m_{211}^h & m_{121}^h & m_{112}^h & m_{221}^h & m_{122}^h & m_{212}^h & m_{222}^h \end{pmatrix} \times \begin{pmatrix} b_1 \\ b_2 \\ b_3 \\ b_4 \\ b_5 \\ b_6 \\ b_7 \\ b_8 \end{pmatrix} = \begin{pmatrix} 1 \\ 0 \\ 0 \\ 0 \\ 0 \\ 0 \\ 0 \\ 0 \end{pmatrix}, \quad (4)$$

Note that $\{\mathcal{H}_I(X)\}$ is a partition of unity:

$$\sum_{I \in \Lambda} \mathcal{H}_I(X) = 1 \quad (5)$$

where Λ is the particle index set. It can reproduce the following polynomials exactly, i.e.

$$\sum_{I \in \Lambda} \mathcal{K}_I(X) X_{1I} = X_1 \quad (6)$$

$$\sum_{I \in \Lambda} \mathcal{K}_I(X) X_{2I} = X_2 \quad (7)$$

$$\sum_{I \in \Lambda} \mathcal{K}_I(X) X_{3I} = X_3 \quad (8)$$

$$\sum_{I \in \Lambda} \mathcal{K}_I(X) X_{1I} X_{2I} = X_1 X_2 \quad (9)$$

$$\sum_{I \in \Lambda} \mathcal{K}_I(X) X_{2I} X_{3I} = X_2 X_3 \quad (10)$$

$$\sum_{I \in \Lambda} \mathcal{K}_I(X) X_{3I} X_{1I} = X_3 X_1 \quad (11)$$

$$\sum_{I \in \Lambda} \mathcal{K}_I(X) X_{1I} X_{2I} X_{3I} = X_1 X_2 X_3 \quad (12)$$

A detailed proof of the above properties can be found in Liu et al. [24]. To this end, the reproducing kernel particle interpolation can be put into a simple form

$$u_i^p(X) = \sum_{I \in \Lambda} \mathcal{K}_I(X) u_{iI}, \quad i = 1, 2, 3 \quad (13)$$

To visualize the spatial profile of such shape function, we plot a single shape function and its three first order derivatives in Fig. 1. Even though the support size of the shape function is a rectangular box, one may observe from Fig. 1 that the domain of non-zero value of the shape function tends to be a sphere, and the domain of non-zero value of the derivatives of the shape function are two connected spherical regions; this implies that the spatial distribution of RKPM shape function is almost “isotropic”, which is a desired property in some situations, such as shear band simulation. In Fig. 1a, we take the first octant out from the quasi-sphere region, and one can see that the shape function reaches its maximum at the corresponding particle, i.e. the center. In each of Fig. 1b–d, we take one quadrant out to see the orientation and the distribution of the derivatives.

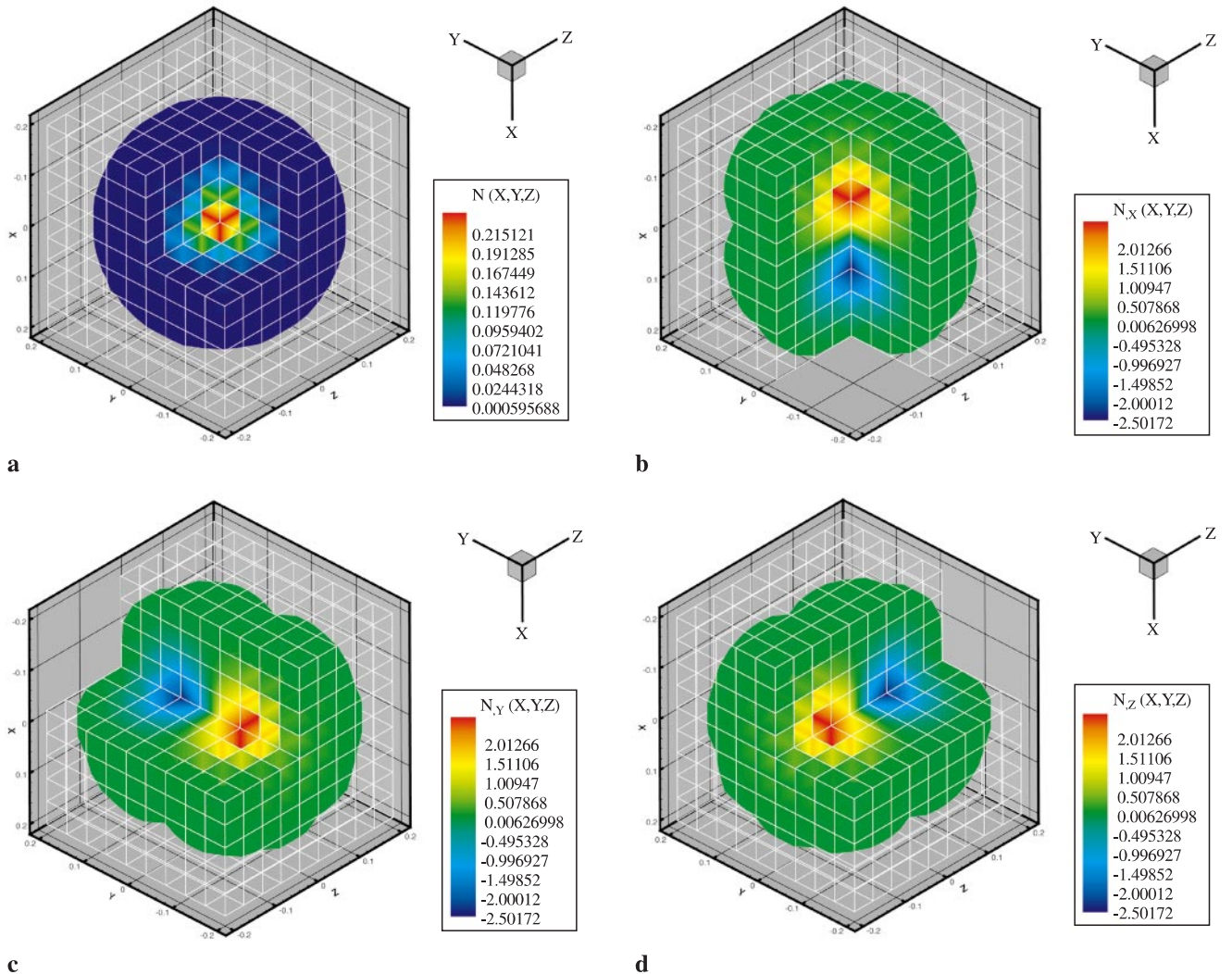


Fig. 1a–d. 3-D RKPM/meshfree shape function and its first derivatives generated by the tri-linear polynomial basis, $\mathbf{P}(X) = (1, X_1, X_2, X_3, X_1 X_2, X_2 X_3, X_3 X_1, X_1 X_2 X_3)$. **a** The shape function, $\mathcal{K}_I(X)$, **b** The derivative, $\mathcal{K}_{I,X_1}(X)$, **c** The derivative, $\mathcal{K}_{I,X_2}(X)$, **d** The derivative $\mathcal{K}_{I,X_3}(X)$

2.2

An explicit meshfree Galerkin formulation

Because of its simplicity, explicit computation is very attractive in practice, especially for large scale computations of large deformation problems. However, most inelastic materials are nearly incompressible, which poses some technical difficulties in displacement based linear finite element formulation. For instance, the displacement based Galerkin formulation may induce volumetric locking, which leads to failure in computations. In practice, such difficulty is usually handled by either mixed formulation, or a reduced integration scheme, e.g. the enhanced strain methods (Simo and Rifai [30]). In doing so, one may have to develop special incompatible elements, which, to certain extent, complicates numerical implementation since they are usually not suitable for explicit computations. For example, an immediate difficulty is how to adapt the mixed formulations for quadrilateral (or hexahedral) grids. In this paper, we propose a meshfree, explicit, total Lagrangian formulation, which is believed to have certain capacity to remedy some algorithmic deficiencies mentioned above.

The equation of motion is

$$\sigma_{jij} + b_i = \rho \dot{v}_i \quad (14)$$

where σ is Cauchy stress, \mathbf{b} is the body force per unit volume, ρ is the density of the material, and \mathbf{v} is the velocity of the continuum. For simplicity, the boundary conditions are specified with respect to the original configuration,

$$\mathbf{P} \cdot \mathbf{n}_0 = \mathbf{T}^0, \quad \forall X \in \Gamma_X^T \quad (15)$$

$$\mathbf{u} = \mathbf{u}^0, \quad \forall X \in \Gamma_X^u \quad (16)$$

where \mathbf{P} is the first Piola-Kirchhoff stress tensor, and $\Gamma_X^T \cup \Gamma_X^u = \partial\Omega_X$.

We start with a weighted residual form in the sense of Petrov-Galerkin,

$$\int_{\Omega_x} \{ \rho \ddot{u}_i - \sigma_{jij} - b_i \} \delta u_i \, d\Omega_x = 0, \quad (17)$$

then the following weak form can be derived,

$$\begin{aligned} \int_{\Omega_x} \rho_0 \ddot{u}_i \delta u_i \, d\Omega_x + \int_{\Omega_x} P_{ji} \delta F_{ji}^T \, d\Omega_x - \int_{\Omega_x} B_i \delta u_i \, d\Omega_x \\ - \int_{\Gamma_X^T} T_i^0 \delta u_i \, d\Gamma - \int_{\Gamma_X^u} T_i \delta u_i \, d\Gamma = 0. \end{aligned} \quad (18)$$

Assume the discrete trial, and weighting functions have the form

$$u_i^h(X, t) = \sum_{I=1}^{NP} N_I(X) \tilde{u}_{iI}(t). \quad (19)$$

$$\delta u_i^h(X, t) = \sum_{I=1}^{NP} N_I(X) \delta \tilde{u}_{iI}(t). \quad (20)$$

Unlike FE approximation, the RKPM interpolant has a shortcoming: that is its inability to represent essential boundary condition via boundary value interpolation, i.e.

$$\tilde{u}_{iI}(t) \neq u_i^0(X_I, t), \quad \forall X_I \in \Gamma^u \quad (21)$$

$$\delta \tilde{u}_{iI}(t) \neq 0, \quad \forall X_I \in \Gamma^u \quad (22)$$

and hence $\delta u^h(X) \neq 0, \forall X \in \Gamma^u$. This is reflected in the weak form (18) as the extra term, $\int_{\Gamma_X^u} T_i \delta u_i \, d\Gamma$, which is a nuisance because the traction force, T_i , is unknown on the essential boundary. Before proceeding further, we have to modify the meshfree interpolant such that the essential boundary conditions are taken into account in the interpolation scheme. To do so, we distribute N_b number of particles on the boundary Γ^u , and enforce the meshfree interpolant, $u^h(X, t) \in \text{span}\{N_I(X) \mid I = 1, \dots, NP\}$, such that

$$u_i^h(X_I, t) = u_i^0(X_I, t) =: g_i(X_I, t), \quad I = 1, \dots, N_b \quad (23)$$

For simplicity, we denote $g_{iI}(t) := g_i(X_I, t)$, $I = 1, \dots, N_b$. Let $N_{nb} := NP - N_b$. The particles and the associated discrete field variables can be separated into two parts, each of them are marked with superscript b and nb ,

$$\begin{aligned} u_i^h(X, t) &= \sum_{I=1}^{NP} N_I(X) \tilde{u}_{iI}(t) \\ &= \sum_{I=1}^{N_b} N_I^b(X) \tilde{u}_{iI}^b(t) + \sum_{I=1}^{N_{nb}} N_I^{nb}(X) \tilde{u}_{iI}^{nb}(t) \\ &= \mathbf{N}^b(X) \tilde{\mathbf{u}}_i^b(t) + \mathbf{N}^{nb}(X) \tilde{\mathbf{u}}_i^{nb}(t) \end{aligned} \quad (24)$$

where

$$\mathbf{N}^b(X) := \{N_1^b(X), \dots, N_{N_b}^b(X)\}, \quad (25)$$

$$\tilde{\mathbf{u}}_i^b(t) := \{\tilde{u}_{i1}^b(t), \dots, \tilde{u}_{iN_b}^b(t)\};$$

$$\mathbf{N}^{nb}(X) := \{N_1^{nb}(X), \dots, N_{N_{nb}}^{nb}(X)\}, \quad (26)$$

$$\tilde{\mathbf{u}}_i^{nb}(t) := \{\tilde{u}_{i1}^{nb}(t), \dots, \tilde{u}_{iN_{nb}}^{nb}(t)\}.$$

Let

$$\mathbf{D}^b := \begin{pmatrix} \vdots & & \\ \cdots & N_I^b(X_J) & \cdots \\ \vdots & & \end{pmatrix}^{N_b \times N_b} \quad (27)$$

$$\mathbf{D}^{nb} := \begin{pmatrix} \vdots & & \\ \cdots & N_I^{nb}(X_J) & \cdots \\ \vdots & & \end{pmatrix}^{N_b \times N_{nb}} \quad (28)$$

Thus the enforced discrete essential conditions, (23), may read as follows

$$\mathbf{D}^b \tilde{\mathbf{u}}_i^b(t) = \mathbf{g}_i(t) - \mathbf{D}^{nb} \tilde{\mathbf{u}}_i^{nb}(t) \quad (29)$$

$$\mathbf{D}^b \delta \tilde{\mathbf{u}}_i^b(t) = -\mathbf{D}^{nb} \delta \tilde{\mathbf{u}}_i^{nb}(t) \quad (30)$$

after inverting matrix \mathbf{D}^b ,

$$\tilde{\mathbf{u}}_i^b(t) = (\mathbf{D}^b)^{-1} \mathbf{g}_i(t) - (\mathbf{D}^b)^{-1} \mathbf{D}^{nb} \tilde{\mathbf{u}}_i^{nb}(t) \quad (31)$$

$$\delta \tilde{\mathbf{u}}_i^b(t) = -(\mathbf{D}^b)^{-1} \mathbf{D}^{nb} \delta \tilde{\mathbf{u}}_i^{nb}(t) \quad (32)$$

Substitution (31) back into (24) yields

$$\begin{aligned} u_i^h(X, t) &= \sum_{I=1}^{NP} N_I(X) \tilde{u}_{iI}(t) \\ &= \mathbf{N}^b(X) (\mathbf{D}^b)^{-1} \mathbf{g}_i(t) \\ &\quad + (\mathbf{N}^{nb}(X) - \mathbf{N}^b(X) (\mathbf{D}^b)^{-1} \mathbf{D}^{nb}) \tilde{\mathbf{u}}_i^{nb}(t) \end{aligned} \quad (33)$$

$$\delta u_i^h(X, t) = (\mathbf{N}^{nb}(X) - \mathbf{N}^b(X)(\mathbf{D}^b)^{-1}\mathbf{D}^{nb})\delta \tilde{\mathbf{u}}_i^{nb}(t) \quad (34)$$

Obviously, for $X_I \in \Gamma^u$, $I = 1, \dots, N_b$,

$$u_i^h(X_I, t) = g_{il}(t) ; \quad (35)$$

$$\delta u_i^h(X_I, t) = 0, \quad I = 1, 2, \dots, N_b \quad (36)$$

Equation (33) can be also interpreted as the transformation of shape functions, i.e.

$$\begin{aligned} u_i^h(X, t) &= \sum_{I=1}^{N_b} W_I^b(X) u_{iI}^b(t) + \sum_{I=1}^{N_{nb}} W_I^{nb} \tilde{u}_{iI}^{nb}(t) \\ &= \mathbf{W}^b(X) \mathbf{u}_i^b + \mathbf{W}^{nb}(X) \tilde{\mathbf{u}}_i^{nb} \end{aligned} \quad (37)$$

where $\mathbf{W}^b(X) := \mathbf{N}^b(X)(\mathbf{D}^b)^{-1}$, and $\mathbf{W}^{nb}(X) := [\mathbf{N}^{nb}(X) - \mathbf{N}^b(X)(\mathbf{D}^b)^{-1}\mathbf{D}^{nb}]$. One may notice that the new shape functions in (37) at essential boundary possess the Kronecker-delta, or interpolation property. The justification of such enforcement of essential boundary is discussed in detail in Li and Liu [15]. The modified reproducing kernel interpolant,

$$u_i^h(X, t) = \sum_{I=1}^{NP} N_I(X) \tilde{u}_{iI}(t) , \quad (38)$$

is used as both trial and weighting functions in a quasi Bubnov-Galerkin formulation. Note that here $\{\tilde{u}_{iI}(t)\} = \{\tilde{u}_{iI}^b(t)\} \cup \{\tilde{u}_{iI}^{nb}(t)\}$, and $\{\tilde{u}_{iI}^b(t)\}$ and $\{\tilde{u}_{iI}^{nb}(t)\}$ are related through Eq. (31). Then the discrete equations of motion can be put into the standard form,

$$\mathbf{M}\ddot{\mathbf{u}} + \mathbf{f}^{\text{int}} = \mathbf{f}^{\text{ext}} \quad (39)$$

where \mathbf{M} is the mass matrix, and

$$\mathbf{f}_I^{\text{ext}} = \int_{\Gamma_x^r} T_i^0(X, t) N_I(X) \mathbf{e}_i d\Gamma + \int_{\Omega_x} B_i(X, t) N_I(X) \mathbf{e}_i d\Omega \quad (40)$$

$$\mathbf{f}_I^{\text{int}} = \int_{\Omega_x} P_{ji} \frac{\partial N_I}{\partial X_j} \mathbf{e}_i d\Omega \quad (41)$$

The only place that the meshfree explicit scheme differs from FEM explicit scheme is that in each time iteration one has to enforce, or update the essential boundary conditions in the following manner,

$$\tilde{\mathbf{u}}_i^b(t) = (\mathbf{D}^b)^{-1} (\mathbf{g}_i(t) - \mathbf{D}^{nb} \tilde{\mathbf{u}}_i^{nb}(t)) \quad (42)$$

$$\dot{\tilde{\mathbf{u}}}_i^b(t) = (\mathbf{D}^b)^{-1} (\dot{\mathbf{g}}_i(t) - \mathbf{D}^{nb} \dot{\tilde{\mathbf{u}}}_i^{nb}(t)) \quad (43)$$

As shown by Li and Liu [15], the essential boundary condition enforcement is accurate, if there are enough particles distributed along the essential boundary. Readers can also find some discussions on enforcing the essential boundary conditions for meshfree methods in Güther and Liu [9].

3

Tension of a thin viscoplastic sheet

The first problem computed is a tension test of thin sheet specimen which is made of elasto-viscoplastic material. The prescribed displacement/velocity boundary condition is imposed at both ends of the specimens as shown in Fig. 2.

Our computations is motivated by finding the shear band evolution in thin metal sheet stretching. For this purpose, an elasto-viscoplastic solid is chosen in computational simulations since this material model is well regularized, and hence the mathematical problem is well-posed. For the original homogeneous specimen, the shear band formation can be triggered by embedding imperfections, or inhomogeneities into the virgin specimen (See Pan [27], Shawki and Clifton [29], and Needleman [26]).

The rate form constitutive equation reads as follows

$$\overset{\nabla}{\boldsymbol{\tau}} := \mathbf{C} : (\mathbf{d} - \mathbf{d}^{vp}) , \quad (44)$$

where \mathbf{C} is the spatial elastic constant, and the Jaumann rate of Kirchhoff stress, $\overset{\nabla}{\boldsymbol{\tau}}$, is defined as

$$\overset{\nabla}{\boldsymbol{\tau}} = \dot{\boldsymbol{\tau}} - \boldsymbol{\omega} \boldsymbol{\tau} + \boldsymbol{\tau} \boldsymbol{\omega} \quad (45)$$

and

$$\mathbf{d} := d_{ij} \mathbf{e}_i \otimes \mathbf{e}_j, \quad d_{ij} := \frac{1}{2} \left(\frac{\partial v_i}{\partial x_j} + \frac{\partial v_j}{\partial x_i} \right) \quad (46)$$

$$\mathbf{w} := w_{ij} \mathbf{e}_i \otimes \mathbf{e}_j, \quad w_{ij} := \frac{1}{2} \left(\frac{\partial v_i}{\partial x_j} - \frac{\partial v_j}{\partial x_i} \right) \quad (47)$$

A von Mises type viscoplastic solid is considered

$$\mathbf{s} = \boldsymbol{\tau} - \frac{1}{3} \text{tr}(\boldsymbol{\tau}) \quad (48)$$

$$\mathbf{s}' = \mathbf{s} - \boldsymbol{\alpha} \quad (49)$$

$$f(\mathbf{s}', \kappa) = \bar{\sigma} - \kappa = 0 \quad (50)$$

$$\bar{\sigma}^2 = \frac{3}{2} \mathbf{s}' : \mathbf{s}' , \quad (51)$$

$$\mathbf{P} = \frac{3 \mathbf{s}'}{2 \bar{\sigma}} \quad (52)$$

$$\mathbf{d}^{vp} := \dot{\bar{\epsilon}}(\bar{\sigma}, \bar{\epsilon}) \frac{\partial f}{\partial \tau_{ij}}, \quad \text{or} \quad \mathbf{d}^{vp} = \dot{\bar{\epsilon}}(\bar{\sigma}, \bar{\epsilon}) \mathbf{P} \quad (53)$$

$$\dot{\bar{\epsilon}} := \int_0^t \left[\frac{\mathbf{d}^{vp} : \mathbf{d}^{vp}}{\mathbf{P} : \mathbf{P}} \right]^{1/2} dt \quad (54)$$

The power law that governs the viscoplastic flow is described as

$$\dot{\bar{\epsilon}} := \dot{\epsilon}_0 \left[\frac{\bar{\sigma}}{g(\bar{\epsilon})} \right]^{1/m}, \quad g(\bar{\epsilon}) = \sigma_0 \frac{[1 + \bar{\epsilon}/\epsilon_0]^N}{1 + (\bar{\epsilon}/\epsilon_1)^2} . \quad (55)$$

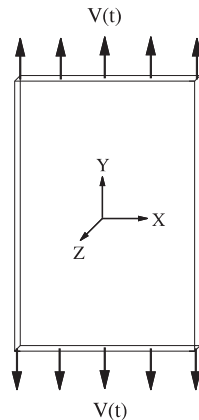


Fig. 2. Problem statement: a thin sheet under tension

where m is the power index. The back stress evolution law is taken as a finite strain form of the Prager-Ziegler relation,

$$\overset{\nabla}{\boldsymbol{\alpha}} = b\mathbf{d}^{vp} \quad (56)$$

In computations, an explicit predict-correct time integration scheme is adopted; and the constitutive update follows largely from tangent modulus method by Peirce et al. [28]; nonetheless, small modification has been made, which is summarized in Box 1. A detailed discussion to extend the tangent modulus method to the case of adiabatic, thermo-viscoplastic material has been carried out in [14]. Choosing $t_{n+\theta} \in [t_n, t_{n+1}]$, $\theta \in [0, 1]$,

Box 1(a) Kinematic prediction

$$\begin{aligned} \mathbf{v}_{n+1}^{\text{trial}} &= \mathbf{v}_n + \Delta t \mathbf{a}_n \\ \mathbf{v}_\theta &= (1 - \theta)\mathbf{v}_n + \theta \mathbf{v}_{n+1}^{\text{trial}} = \mathbf{v}_n + \theta \Delta t \mathbf{a}_n \\ \mathbf{u}_\theta &= (1 - \theta)\mathbf{v}_n + \theta \mathbf{u}_{n+1} = \mathbf{u}_n + \Delta t \theta \mathbf{v}_n + \theta^2 \Delta t^2 \mathbf{a}_n \\ \mathbf{L}_\theta &= \mathbf{v}_\theta \overset{\leftarrow}{\nabla} \mathbf{x} = \left(\mathbf{v}_\theta \overset{\leftarrow}{\nabla} \mathbf{x} \right) \cdot \mathbf{F}_{n+1}^{-1} \\ \mathbf{d}_\theta &= \frac{1}{2} (\mathbf{L}_\theta + \mathbf{L}_\theta^T) \\ \mathbf{w}_\theta &= \frac{1}{2} (\mathbf{L}_\theta - \mathbf{L}_\theta^T) \end{aligned}$$

Box 1(b) State variable update

$$\begin{aligned} \mathbf{P}_\theta &\approx \mathbf{C} : \mathbf{p}_n \\ \mathbf{Q}_\theta &\approx \left. \frac{\partial \dot{\bar{\epsilon}}}{\partial \bar{\sigma}} \right|_n \mathbf{P}_n \\ \bar{H}_\theta &\approx - \left. \frac{\partial \dot{\bar{\epsilon}}}{\partial \bar{\epsilon}} \right|_n + \left. \frac{\partial \dot{\bar{\epsilon}}}{\partial \bar{\sigma}} \right|_n (b\mathbf{p} : \mathbf{p} + \mathbf{p} : \mathbf{L} : \mathbf{p})_n \\ h_\theta &\approx \bar{H}_\theta / (\partial \dot{\bar{\epsilon}} / \partial \bar{\sigma})_n \\ \zeta_\theta &\approx \theta \Delta t \left(\frac{\partial \dot{\bar{\epsilon}}}{\partial \bar{\sigma}} \right)_n h_\theta \\ \mathbf{C}_\theta^{\text{tan}} &= \mathbf{C} - \left(\frac{\zeta}{1 + \zeta} \frac{1}{h} \right)_\theta \mathbf{P}_\theta \otimes \mathbf{P}_\theta \\ \dot{\bar{\epsilon}}_\theta &\approx \frac{\dot{\bar{\epsilon}}_n}{1 + \zeta_n} + \frac{1}{\bar{H}_\theta} \frac{\zeta_\theta}{1 + \zeta_\theta} \mathbf{Q}_\theta : \mathbf{d}_\theta \\ \overset{\nabla}{\boldsymbol{\tau}}_\theta &= \mathbf{C}_\theta^{\text{tan}} : \mathbf{d}_\theta - \frac{\dot{\bar{\epsilon}}_\theta}{1 + \zeta_\theta} \mathbf{P}_\theta \\ \dot{\boldsymbol{\tau}}_\theta &\approx \overset{\nabla}{\boldsymbol{\tau}}_\theta + \mathbf{w}_\theta \cdot \boldsymbol{\tau}_n + \boldsymbol{\tau}_n \cdot \mathbf{w}_\theta^T \\ \bar{\epsilon}_{n+1} &= \bar{\epsilon}_n + \dot{\bar{\epsilon}}_\theta \Delta t \\ \boldsymbol{\tau}_{n+1} &= \boldsymbol{\tau}_n + \dot{\boldsymbol{\tau}}_\theta \Delta t \\ \mathbf{d}_\theta^{vp} &= \dot{\bar{\epsilon}}_\theta \mathbf{P}_n \\ \overset{\nabla}{\boldsymbol{\alpha}}_\theta &= b\mathbf{d}_\theta^{vp} \\ \dot{\boldsymbol{\alpha}}_\theta &= \overset{\nabla}{\boldsymbol{\alpha}}_\theta + \mathbf{w}_\theta \cdot \boldsymbol{\alpha}_n + \boldsymbol{\alpha}_n \cdot \mathbf{w}_\theta^T \\ \boldsymbol{\alpha}_{n+1} &= \boldsymbol{\alpha}_n + \dot{\boldsymbol{\alpha}}_\theta \Delta t \end{aligned}$$

Based on the updated Kirchhoff stress, one can easily calculate the first Piola-Kirchhoff stress, $P_{Ij}(X, t_{n+1})\mathbf{E}_I \otimes \mathbf{e}_j$, at $t = t_{n+1}$. Then one may calculate internal force, $\mathbf{f}_{n+1}^{\text{int}}$ based on Eq. (41), and finally proceed to the kinematic correction,

Box 1(c) Kinematic correction

$$\begin{aligned} \mathbf{a}_{n+1} &= \mathbf{M}^{-1} (\mathbf{f}_{n+1}^{\text{ext}} - \mathbf{f}_{n+1}^{\text{int}}) \\ \mathbf{v}_{n+1} &= \mathbf{v}_n + \Delta t ((1 - \theta)\mathbf{a}_n + \theta \mathbf{a}_{n+1}) \end{aligned} \quad (57)$$

The numerical results obtained from tension test are displayed in Fig. 3a–d. The specimen used in the computation is 2 mm in width; 4 mm in length; and 0.2 mm in thickness. The maximum spatial aspect ratio of the specimen is 20. There are five layers of particles distributed along the thickness direction. A total 16,165 particles are used in computations. A unusual phenomenon is observed in our computations: one may observe that in Fig. 3c and d there are apparently a second strain “concentration region” inside the original shear band. It seems to us that its appearance is due to the fact that the specimen is very thin, and unlike the plane strain problem there is no additional material available in the thickness direction to compensate the axial tensile stretch. Thus, the original shear band grow wider and wider. On the other hand, within the original shear band there is homogeneous uniform high strain gradient plateau thus the imperfection in the center may initiate a second shear localization. A further investigation may be needed before an positive statement can be made for existence such “secondary shear band, or shear localization”. For detailed computation procedures on 3-D shear-band simulation, readers are referred to a recent paper by Li and Liu [15].

4

Large deformation of hyperelastic thin shells

For hyperelastic materials, we consider the modified Mooney-Rivlin material (Fried and Johnson [8]), whose constitutive relations are outlined at below.

4.1

Hyperelastic constitutive equation

For hyperelastic materials, it is assumed that there exists a strain energy density potential function. For isotropic homogeneous nonlinear elastic materials, the energy density function can be represented by the invariants of the strain measure, for instance,

$$W = W(\mathbf{F}) = W(\mathbf{C}) = W(I_1, I_2, I_3) \quad (58)$$

where \mathbf{F} is the deformation gradient; and $\mathbf{C} = \mathbf{F}^T \cdot \mathbf{F}$ is the right Cauchy-Green deformation tensor; and the three invariants of the right Cauchy-Green tensor are defined as

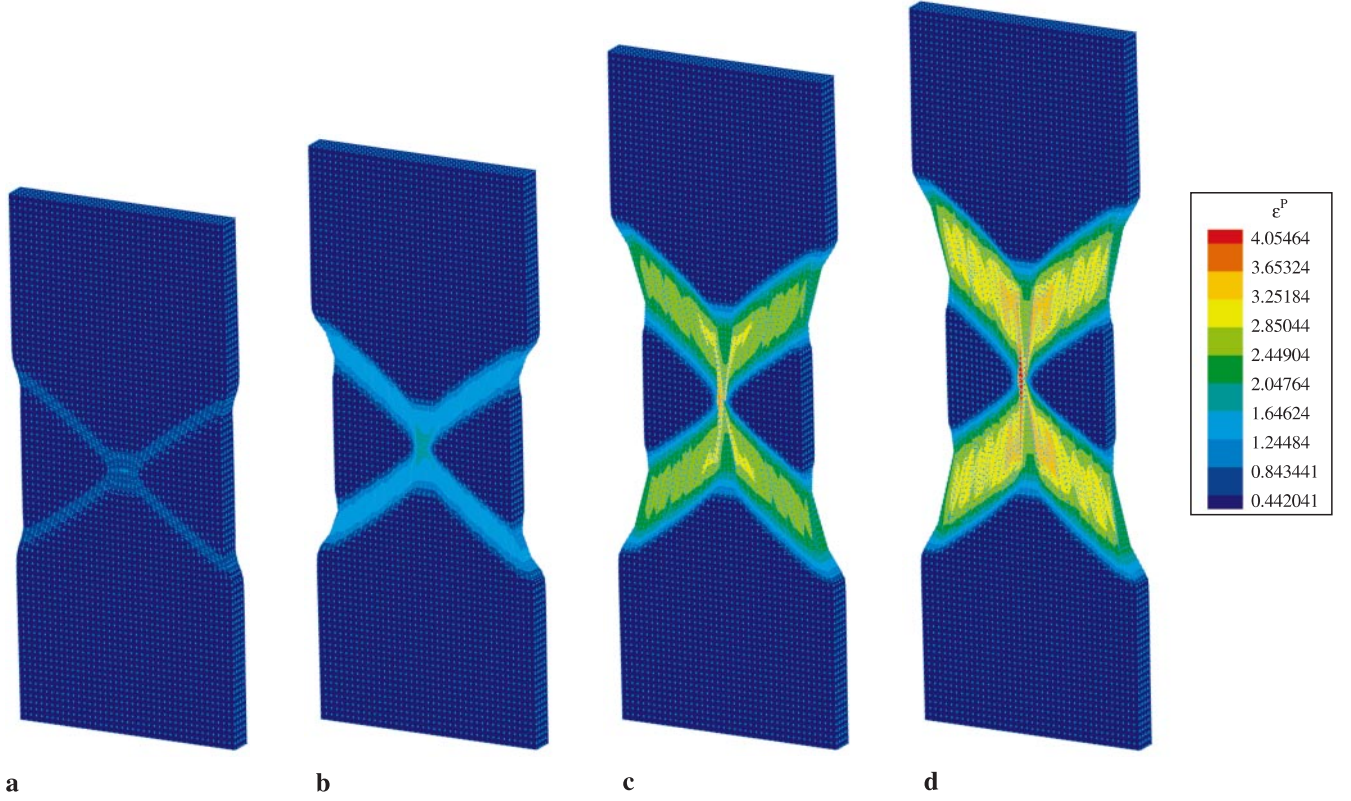


Fig. 3a-d. Contours of viscoplastic strain in a thin sheet under tension. **a** $t = 1.0 \times 10^{-5}$ s, **b** $t = 2.0 \times 10^{-5}$ s, **c** $t = 4.0 \times 10^{-5}$ s, **d** $t = 5.0 \times 10^{-5}$ s

$$I_1 = \text{tr}(\mathbf{C}) \quad (59)$$

$$I_2 = \frac{1}{2} [(\text{tr}(\mathbf{C}))^2 - \text{tr}(\mathbf{C}^2)] \quad (60)$$

$$I_3 = \det(\mathbf{C}) \quad (61)$$

For the modified Mooney-Rivlin material, the strain energy density function, W , is explicitly given by

$$W = C_1(I_1 - 3I_3^{1/3}) + C_2(I_2 - 3I_3^{2/3}) + \frac{1}{2}\lambda(\ln I_3)^2 \quad (62)$$

where the constants, C_1, C_2 and λ are material constants. The corresponding constitutive relations can be expressed in terms of the second Piola-Kirchhoff stress tensor, \mathbf{S} , and the invariants of right Cauchy-Green tensor,

$$\mathbf{S} = 2[(C_1 + C_2I_1)\mathbf{I} - C_2\mathbf{C} - (C_1I_3^{1/3} + 2C_2I_3^{2/3} - \lambda \ln I_3)\mathbf{C}^{-1}] \quad (63)$$

In actual computation, after the second Piola-Kirchhoff stress tensor is obtained, the first Piola-Kirchhoff tensor can be immediately computed as $\mathbf{P} = \mathbf{S} \cdot \mathbf{F}^T$, which can then be substituted into the weak form (18) to calculate the internal nodal force. Since the hyperelastic constitutive law is described by a path-independent, total formulation, the constitutive update is very simple, which is summarized in Box 2.

Box 2 Time integration for the hyperelastic material

$$\tilde{\mathbf{u}}_{n+1} = \mathbf{u}_n + \Delta t \mathbf{v}_n + (1/2 - \beta)\Delta t \mathbf{a}_n$$

$$\tilde{\mathbf{v}}_{n+1} = \mathbf{v}_n + (1 - \gamma)\Delta t \mathbf{a}_n$$

$$\tilde{\mathbf{F}}_{n+1} = \mathbf{I} + \frac{\partial \tilde{\mathbf{u}}_{n+1}}{\partial \mathbf{X}}$$

$$\tilde{\mathbf{C}}_{n+1} = \tilde{\mathbf{F}}_{n+1}^T \tilde{\mathbf{F}}_{n+1}$$

$$\mathbf{S}_{n+1} = 2 \left[(C_1 + C_2 I_1^{n+1}) \mathbf{I} - C_2 \tilde{\mathbf{C}}_{n+1} - (C_1 (I_3^{n+1})^{1/3} + 2C_2 (I_3^{n+1})^{2/3} - \lambda \ln I_3^{n+1}) \tilde{\mathbf{C}}_{n+1}^{-1} \right]$$

$$\mathbf{P}_{n+1} = \mathbf{S}_{n+1} \cdot \tilde{\mathbf{F}}_{n+1}^T$$

$$\mathbf{a}_{n+1} = \mathbf{M}^{-1} \cdot (\mathbf{f}_{n+1}^{\text{ext}} - \mathbf{f}_{n+1}^{\text{int}})$$

$$\mathbf{v}_{n+1} = \tilde{\mathbf{v}}_{n+1} + \gamma \Delta t \mathbf{a}_{n+1}$$

$$\mathbf{u}_{n+1} = \tilde{\mathbf{u}}_{n+1} + \beta \Delta t^2 \mathbf{a}_{n+1}$$

where \mathbf{P}_{n+1} is the first Piola-Kirchhoff stress tensor. In all the numerical examples presented in this paper, we choose $\beta = 0$ and $\gamma = 1/2$.

4.2 The snap-through of a conic shell

In the first numerical example, the large deformation of a conic shell is examined in numerical experiment. The

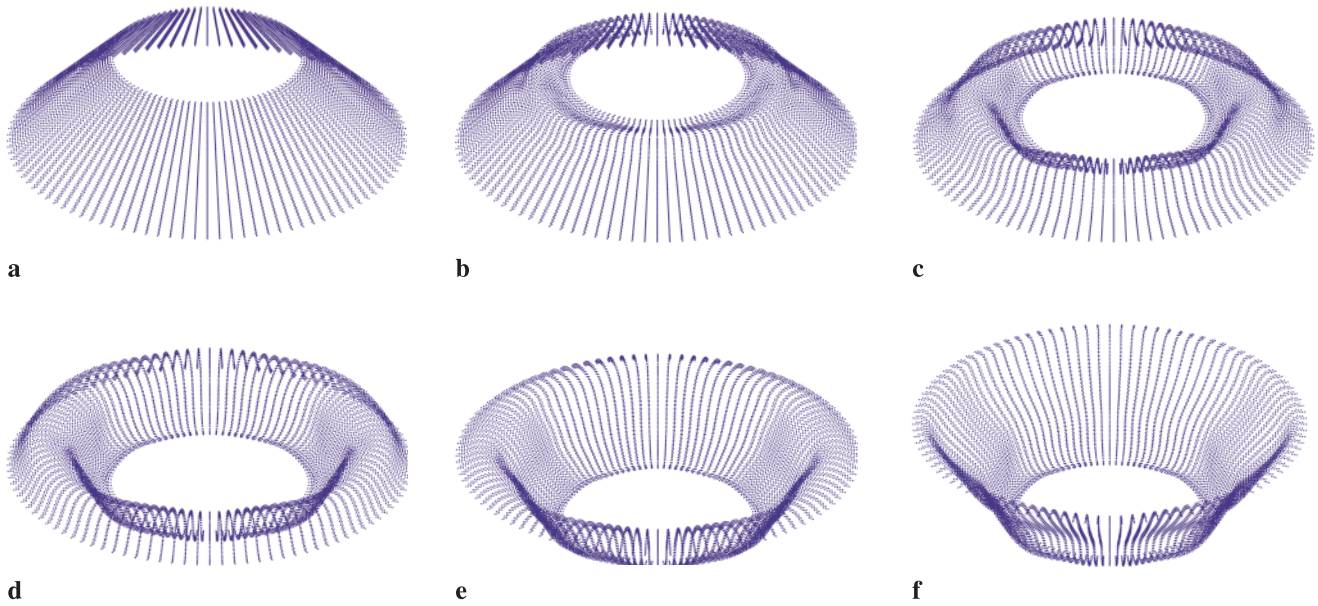


Fig. 4a-f. The snap-through of a conic shell. **a** $t = 2.5 \times 10^{-3}$ s, **b** $t = 5.0 \times 10^{-3}$ s, **c** $t = 9.0 \times 10^{-3}$ s, **d** $t = 10.4 \times 10^{-3}$ s, **e** $t = 8.8 \times 10^{-3}$ s, **f** $t = 10.4 \times 10^{-3}$ s

radius of ring circle at the top of conic shell is 1", and the radius of the ring circle at the bottom of the conic shell is 2". The height of the conic shell is 1", and the thickness of the conic shell is 0.05". A total of 12,300 particles are used in meshfree discretization. Three equally-spaced layers of particles are used in the thickness direction, one on the inner surface, one on the middle surface, and the last one on the out surface. The initial density of the rubber shell is, $\rho_0 = 1.4089 \times 10^{-4}$ (slug) and the material constants are $C_1 = 18.35$ (psi), $C_2 = 1.468$ (psi) and $\lambda = 1.468 \times 10^3$ (psi). In computations, the time increment is chosen as $\Delta t = 2.0 \times 10^{-6}$ s, and 5,200 steps are used for the results shown in Fig. 4.

In the computation, we fixed the bottom edge of the conic shell, i.e. the built-in condition is imposed for the bottom edge; and we control the vertical movement of upper edge such that it drags the whole shell structure down and inward. At the end of the computation, the conic shell turns inside out completely. In Fig. 4, several snapshots are taken to form a deformation sequence. The deformation process is a truly large deformation event, which involves with both physical nonlinearity as well as geometry nonlinearity. Such deformation process belongs to a so-called "snap-through" instability problem because the reaction force/resultant at top edge is alternating with the increasing (or decreasing) of vertical displacement of the top edge.

Compared to the published results of finite element simulations in using degenerated continuum approach, beside the radial buckling mode, one may find additional circumferential buckling mode in our direct 3-D meshfree simulation, which is an indirect evidence of improved accuracy, because circumferential buckling modes may not be observed in finite element simulations based on the degenerated continuum approach (e.g. Basar and Itskov [3]).

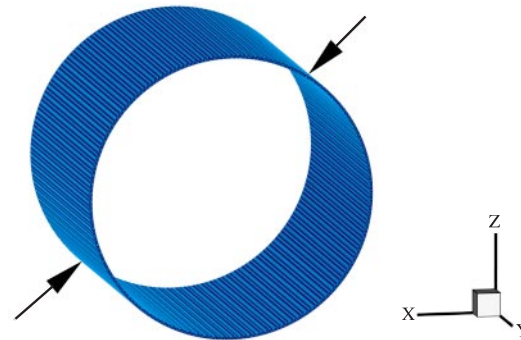


Fig. 5. Model problem: Pinched cylinder

4.3 The pinched cylindrical shell

This problem resembles one of benchmark problems in the so-called standard problem set testing finite element accuracy proposed by MacNeal and Harder [25]. In the original benchmark problem, two concentrated point forces are applied to the cylindrical shell at opposite direction, whereas in our case, we prescribe and control the radial displacement of two opposite particles on the out-surface at the middle section of the shell.

The cylindrical shell has the radius of 1", height 2" and thickness 0.02". Again three layer of particles distributed along the thickness direction. A total of 30,300 particles are used in discretization. The central difference algorithm is chosen in temporal integration. The time increment is $\Delta t = 0.5 \times 10^{-6}$ s, and the total 21,000 time step has been taken to finish the run that is shown in Fig. 6.

From the deformation sequence shown in Fig. 6, one may find that the deformation of the cylindrical shell under pinched loadings is drastic, and apparently, one can

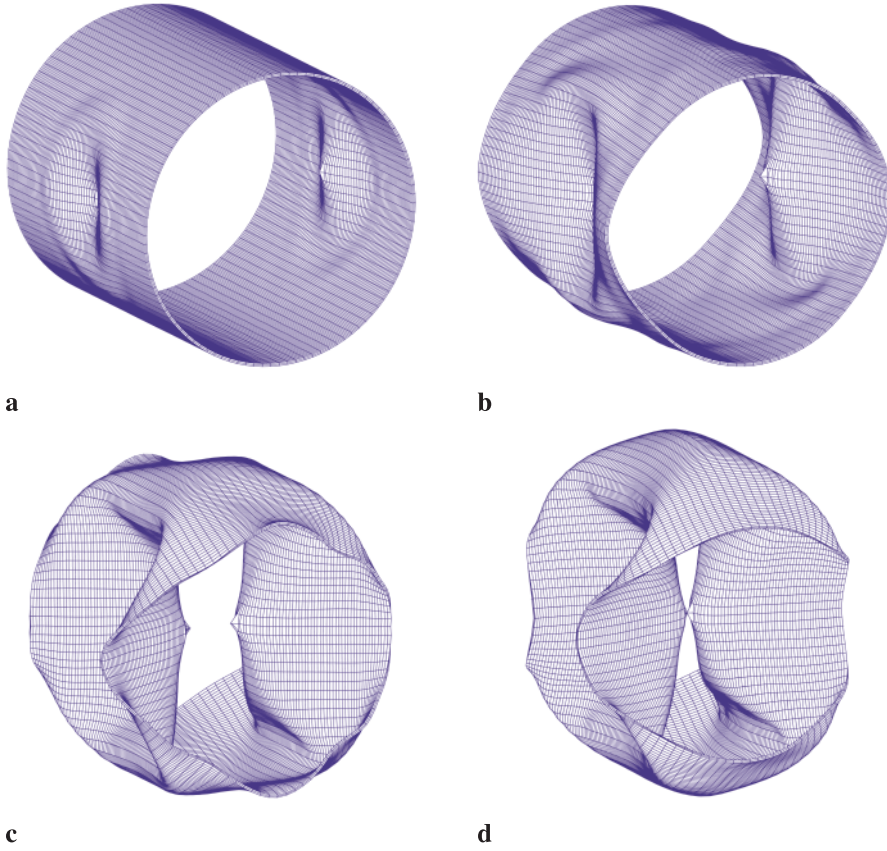


Fig. 6a–d. The deformation sequence of a pinched cylinder. **a** $t = 2.0 \times 10^{-3}$ s, **b** $t = 4.0 \times 10^{-3}$ s, **c** $t = 8.0 \times 10^{-3}$ s, **d** $t = 10.5 \times 10^{-3}$ s

observe the interaction among different buckling modes. At the end of our computation, the two opposite points of inner surface of the cylindrical shell actually come together.

5 Large deformation problems of elasto-plasticity thin shell structures

Another complex issue for nonlinear shell formulation is how to embed inelastic constitutive relation onto manifold. It is usually a nontrivial task to develop an elasto-plastic nonlinear shell theory even for the degenerated approach. Nevertheless, this will not be a problem at all for 3-D direct approach. In this section, the meshfree approach is employed to calculate the thin shell structures that are governed by elasto-plastic constitutive relations. The computational formulas of our computation largely follow from that of Hughes [11], and Simo and Hughes [10].

5.1 J_2 hypoelastic-plastic material at finite strain

A rate form hypoelastic J_2 constitutive relation in finite deformation is considered. The J_2 yield criterion is described as

$$f(\xi, \alpha, e^p) = \|\xi\| - \sqrt{\frac{2}{3}}\kappa(e^p) = 0 \quad (64)$$

$$\mathbf{s} := \boldsymbol{\tau} - \frac{1}{3}\text{tr}(\boldsymbol{\tau})\mathbf{I} \quad (65)$$

$$\xi := \mathbf{s} - \alpha \quad (66)$$

$$e^p = \int_0^t \sqrt{\frac{2}{3}}\|\mathbf{d}^p(\tau)\| d\tau \quad (67)$$

where the Kirchhoff stress $\boldsymbol{\tau} := J\boldsymbol{\sigma}$ and $J = \det \mathbf{F}$.

In this paper, Lie derivative is chosen as the objective rate of stress tensor

$$L_{\mathbf{v}}\boldsymbol{\tau} = \mathbf{c}^{\text{elas}} : [\mathbf{d} - \mathbf{d}^p] \quad (68)$$

where \mathbf{c}^{elas} is the spatial elasticity tensor; and the Lie derivative is defined as

$$L_{\mathbf{v}}\boldsymbol{\tau} := \dot{\boldsymbol{\tau}} - (\nabla_{\mathbf{v}})\boldsymbol{\tau} - \boldsymbol{\tau}(\nabla_{\mathbf{v}})^t = \mathbf{F}\dot{\mathbf{S}}\mathbf{F}^t \quad (69)$$

and for isotropic material, the spatial elastic constants remain isotropic under rigid rotations, $\mathbf{c}^{\text{elas}} = \lambda\mathbf{1} \otimes \mathbf{1} + 2\mu\mathbf{I}$. The plastic flow is described by the classic J_2 associated flow rule,

$$\mathbf{d}^p = \gamma\hat{\mathbf{n}} \quad (70)$$

where

$$\hat{\mathbf{n}} = \frac{\xi}{\|\xi\|} = \frac{\partial f / \partial \boldsymbol{\tau}}{\|\partial f / \partial \boldsymbol{\tau}\|} \quad (71)$$

The plastic loading and unloading condition can be expressed in terms of the Kuhn-Tucker condition

$$\gamma \geq 0, \quad f(\boldsymbol{\tau}, \alpha, e^p) \leq 0, \quad \gamma f(\boldsymbol{\tau}, \alpha, e^p) = 0 \quad (72)$$

The hardening laws are

$$\text{Kinematic hardening: } L_{\mathbf{v}}\alpha = \frac{2}{3}\gamma\mathbf{n} \quad (73)$$

$$\text{Isotropic hardening: } \kappa(e^p) = \sigma_Y + K e^p \quad (74)$$

and

$$\dot{e}^p = \gamma\sqrt{\frac{2}{3}} \quad (75)$$

A standard constitutive update for a rate form hypoelastic J_2 theory at finite strain is adopted (See: Simo and Hughes [10] Chapter 8). For the sake of documentation, a brief description of stress update is outlined at following. Define intermediate configuration between time steps, n and $n + 1$

$$\mathbf{x}_{n+\theta} := (1 - \theta)\mathbf{x}_n + \theta\mathbf{x}_{n+1} . \quad (76)$$

where $\theta \in [0, 1]$. Consequently,

$$\mathbf{F}_{n+\theta} = (1 - \theta)\mathbf{F}_n + \theta\mathbf{F}_{n+1} , \quad (77)$$

and the relative deformation gradients, relative incremental displacement gradient, and the relative Eulerian strain tensor are ($\theta \in [0, 1]$)

$$\mathbf{f}_{n+\theta} := \mathbf{F}_{n+\theta}\mathbf{F}_n^{-1} ; \quad (78)$$

$$\mathbf{h}_{n+\theta} := \frac{\partial \mathbf{u}(\mathbf{x}_{n+\theta})}{\partial \mathbf{x}_{n+\theta}} ; \quad (79)$$

$$\mathbf{e}_{n+\theta} := \frac{1}{2} [\mathbf{1} - (\mathbf{f}_{n+\theta}\mathbf{f}_{n+\theta}^T)^{-1}] \quad (80)$$

and the deformation gradient can be expressed as

$$\mathbf{d}_{n+\theta} = \frac{1}{2\Delta t} [\mathbf{h}_{n+\theta} + \mathbf{h}_{n+\theta}^T + (1 - 2\theta)\mathbf{h}_{n+\theta}^T\mathbf{h}_{n+\theta}] \quad (81)$$

The corresponding return mapping algorithm is summarized as:

Box 3(a) Elastic predictor:

$$\begin{aligned} \tilde{\mathbf{e}}_{n+\theta} &= \Delta t \mathbf{d}_{n+\theta} = \tilde{\mathbf{f}}_{n+\theta}^T \mathbf{e}_{n+1} \tilde{\mathbf{f}}_{n+\theta} \\ \boldsymbol{\tau}_{n+\theta}^{\text{trial}} &= \mathbf{f}_{n+\theta} \boldsymbol{\tau}_n \mathbf{f}_{n+\theta}^T + \mathbf{c}^{\text{elas}} : \tilde{\mathbf{e}}_{n+\theta} \\ \boldsymbol{\alpha}_{n+\theta}^{\text{trial}} &= \mathbf{f}_{n+\theta} \boldsymbol{\alpha}_n \mathbf{f}_{n+\theta}^T \\ \mathbf{e}_{n+\theta}^{\text{p trial}} &= \mathbf{e}_n^{\text{p}} \\ \mathbf{s}_{n+\theta}^{\text{trial}} &= \boldsymbol{\tau}_{n+\theta}^{\text{trial}} - \frac{1}{3} \text{tr}(\boldsymbol{\tau}_{n+\theta}^{\text{trial}}) \\ \boldsymbol{\xi}_{n+\theta}^{\text{trial}} &= \mathbf{s}_{n+\theta}^{\text{trial}} - \boldsymbol{\alpha}_{n+\theta}^{\text{trial}} \\ \mathbf{n}_{n+\theta} &= \frac{\boldsymbol{\xi}_{n+\theta}^{\text{trial}}}{\|\boldsymbol{\xi}_{n+\theta}^{\text{trial}}\|} \end{aligned}$$

and

Box 3(b) Plastic corrector:

$$\begin{aligned} f_{n+\theta}^{\text{trial}} &= \|\boldsymbol{\xi}_{n+\theta}^{\text{trial}}\| - \sqrt{\frac{2}{3}}(\sigma_Y + K e_n^{\text{p}}) \\ \text{If } (f_{n+\theta}^{\text{trial}} > 0) \text{ then} \\ \Delta\gamma &= \frac{|f_{n+\theta}^{\text{trial}}|/2\mu}{1 + K/3\mu} \\ \boldsymbol{\tau}_{n+\theta} &= \boldsymbol{\tau}_{n+\theta}^{\text{trial}} - 2\mu\Delta\gamma\mathbf{n}_{n+\theta} \\ \boldsymbol{\alpha}_{n+\theta} &= \boldsymbol{\alpha}_{n+\theta}^{\text{trial}} + \sqrt{\frac{2}{3}}\Delta\gamma H\mathbf{n}_{n+\theta} \\ \mathbf{e}_{n+\theta}^{\text{p}} &= \mathbf{e}_n^{\text{p}} + \sqrt{\frac{2}{3}}\Delta\gamma \\ \boldsymbol{\xi}_{n+\theta} &= \boldsymbol{\tau}_{n+\theta} - \frac{1}{3} \text{tr}(\boldsymbol{\tau}_{n+\theta}) - \boldsymbol{\alpha}_{n+\theta} \\ \text{Else if } (f_{n+\theta}^{\text{trial}} \leq 0) \text{ then} \\ \Delta\gamma &= 0, \\ \text{Endif} \end{aligned} \quad (82)$$

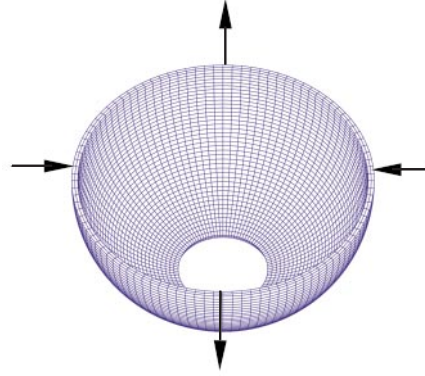


Fig. 7. Hemispherical shell under prescribed displacement, control

In all the computations presented in this paper, only isotropic hardening is considered.

5.2

Hemispheric shell under concentrated loads

Again this is a problem that belongs to the well-known “standard set of problem” testing finite element accuracy (MacNeal and Harder [25]). The dimensions of the hemispherical shell are listed as follows: its radius is 1.0 m, and its thickness is 0.04 m. At the bottom part of the spherical shell, there is a hole, which forms a 18° angle from the center of the spheric shell.

Instead of prescribing concentrated forces on the edge of the spherical shell, we prescribe the displacement at four different locations around the open edge of the hemispherical shell as shown in Fig. 7. The prescribed velocity is 100 m/s. A total of 12,300 particles are used in computation.

In Fig. 8 the plastic strain is plotted on the deformed configuration of the hemispheric shell.

5.3

Crash test of a boxbeam

In this numerical example, we simulate a boxbeam being impacted at one end while the other end being fixed. The rigid impactor is assumed having an infinite mass with a fixed velocity of 20.0 m/s. The Young’s modulus of boxbeam is, $E = 2.1 \times 10^{10}$ Pa; Poisson’s ratio $\mu = 0.3$, the initial yield stress, $\sigma_0 = 1.06 \times 10^9$ Pa. A linear isotropic hardening law is considered in the numerical simulation, $E_t = 4.09 \times 10^7$.

Neglecting contact and frictions between the impactor and the boxbeam, it is assumed that once the impact occurs, the rigid impactor stay with the boxbeam, i.e. the displacements for both x -direction, and y -direction are constrained at the collision surface.

A total of 7,952 particles are used in meshfree discretization. A sequence of intermediate results are displayed in Fig. 10. Only half of the structure is displayed for a better visualization of the buckling mode at interior region. The accuracy of this particular numerical simulation is typically measured by the locations where the buckling mode appears (e.g. Zeng and Combescure [33]). The experiment results show that the first few buckling modes should appear immediately at the impact location. Our numerical

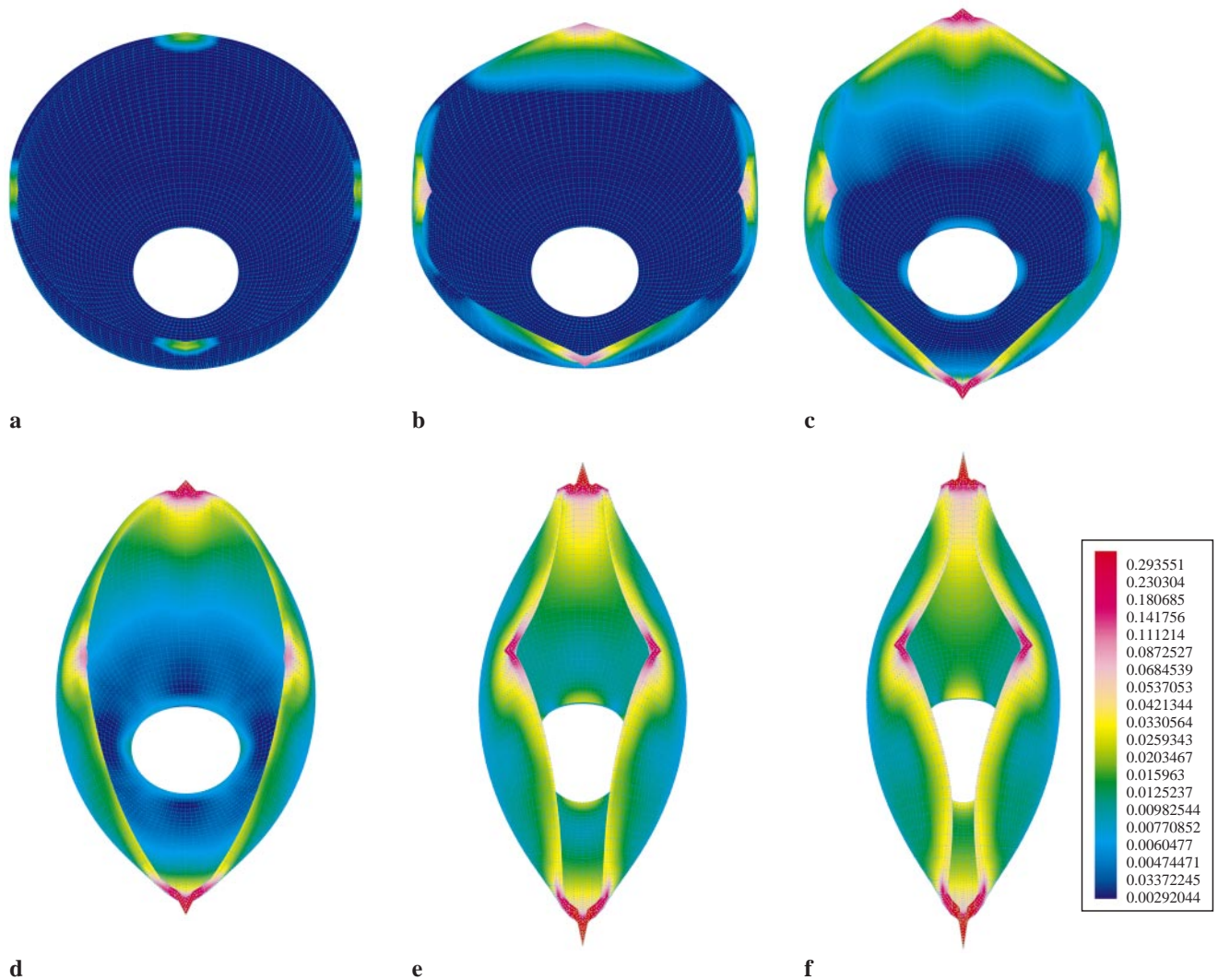


Fig. 8a-f. The plastic strain distribution and deformation sequence of the hemispherical shell. **a** $t = 0.5 \times 10^{-3}$ s, **b** $t = 1.5 \times 10^{-3}$ s, **c** $t = 3.0 \times 10^{-3}$ s, **d** $t = 4.5 \times 10^{-3}$ s, **e** $t = 6.0 \times 10^{-3}$ s, **f** $t = 7.0 \times 10^{-3}$ s

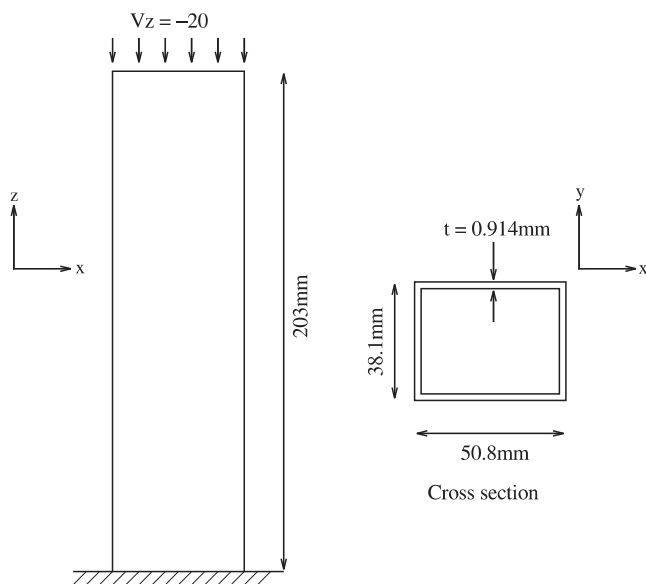


Fig. 9. Crash test of a boxbeam

results give the same prediction. It is noted that only 2 layers of particles are used in the thickness direction, which corresponds to one element in finite element simulation.

Another simulation with both ends being impacted symmetrically, and simultaneously is conducted and the effective plastic strain is plotted on the deformed configuration, which is shown in Fig. 11. One may observe that the maximum plastic deformation occurs at the 90° edge location of the boxbeam, which makes sense because discontinuous curvature of the thin-wall structure could introduce both stress and strain concentrations.

6 A meshfree contact algorithm

In some situations, large deformation of thin shell structures leads to self-contact, at which point, the numerical solution is no longer valid if the self-contact is not under consideration.

In Fig. 12, a deformed shape of a cylindrical shell that is under axial compression is displayed, which is com-

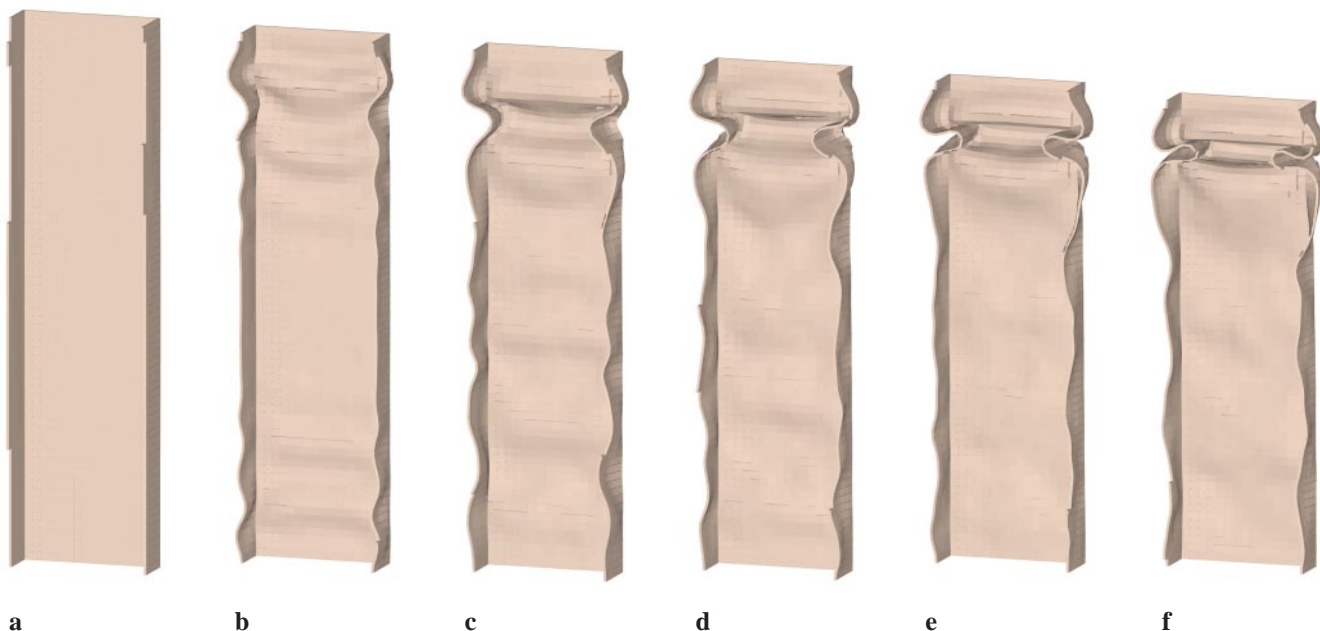


Fig. 10a-h. The deformed configuration of a boxbeam under impact. **a** $t = 0.0$ s, **b** $t = 4.0 \times 10^{-4}$ s, **c** $t = 7.0 \times 10^{-4}$ s, **d** $t = 10.0 \times 10^{-4}$ s, **e** $t = 13.0 \times 10^{-4}$ s, **f** $t = 16.0 \times 10^{-4}$ s

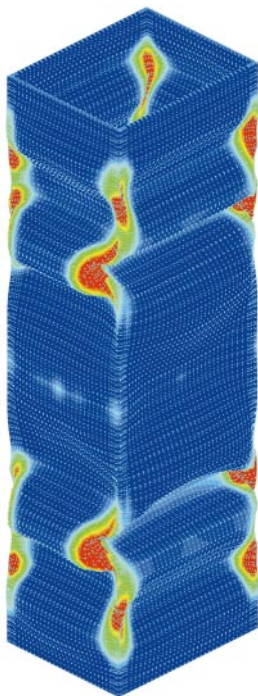


Fig. 11. Effective plastic strain

puted without considering self-contact. Clearly, one can observe, the deformed configuration computed is not realistic, because of inter-penetration of different parts of the cylindrical shell. To correctly simulate large deformation of thin shell structures, it is necessary to develop a meshfree self-contact algorithm. To focus on the main theme of this paper, the newly developed meshfree contact algorithm is briefly introduced here; a detailed exposition of this new meshfree contact algorithm will be reported in a separate paper [18].

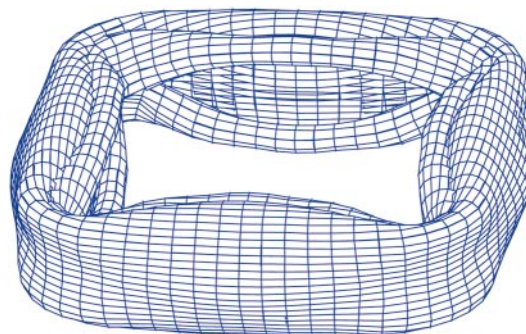
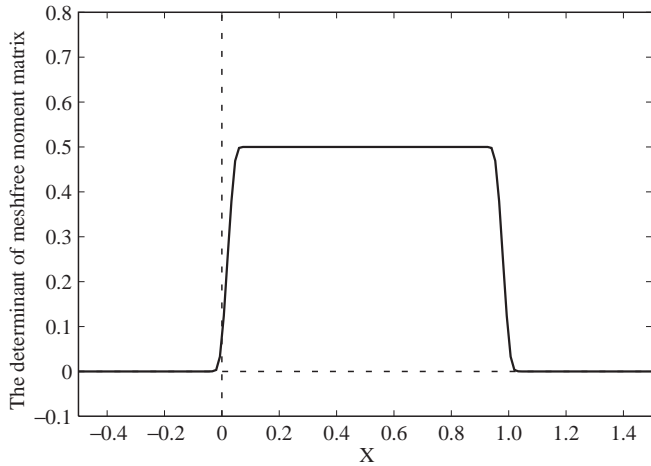


Fig. 12. Computation failure due to self-contact: a cylindrical shell subjected axially compression

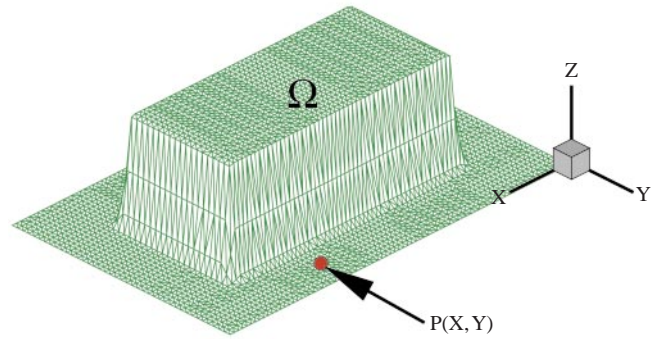
The meshfree contact algorithm relies on an intrinsic property of moving least square interpolant; i.e. at any spatial point within the domain of an admissible meshfree discretization the determinant of the moment matrix at that point will have a positive, finite value, because the moment matrix is positive definite in the domain that yields an admissible meshfree discretization. We may call the set of all such spatial point as the effective domain of the admissible particle distribution. While a point is away from the effective domain, the determinant of the moment matrix ceases to be a finite positive number. To quantify this notion, we start with reviewing the definition of admissible meshfree discretization.

Definition 6.1 (*Admissible meshfree discretization*) (Liu et al. [1997])

Given a positive window function, $\phi(x)$, and a set of independent functions, $\mathcal{P} = \{1, P_2, P_3, \dots, P_m\}$. An admissible meshfree discretization satisfies the following conditions:



a 1-D case



b 2-D case

Fig. 13a, b. The profiles of determinant of the moment matrix in an extended region: **a** $[-0.5, 1.5]$ (the effective domain: $[0.0, 1.0]$); **b** $[-15, 15] \times [5, -15]$ (the effective domain $[-10.0, 10.0] \times [0.0, -10.0]$)

(1) Every particle of the distribution associates with a compact support

$$S_I := \{|X - X_I| \leq R\} \quad (83)$$

and the union of all the compact support, S_I , generates a covering for the domain $\bar{\Omega}$

$$\bar{\Omega} \subset S := \cup_{I=1}^{NP} S_I \quad (84)$$

$$(2) \forall X \in \bar{\Omega}, \exists k > 0, \mathbf{x} \in \cap_{j=1}^k \text{supp}\{\phi(X - X_j)\}, \quad (85)$$

where $N_{\min} \leq k \leq N_{\max}$ and N_{\min}, N_{\max} are given;

(3) The particle distribution should be non-degenerated.

Note: A necessary condition for a non-degenerated particle distribution is: $\max\{m, n + 1\} \leq k$, where m is the order of the polynomial basis, and n is the spatial dimension of domain Ω .

Usually if a spatial point is away from the effective domain of an admissible meshfree discretization, the above necessary condition will soon fail, such that the determinant of the moment matrix will approach to zero, or even become negative, which then provide a natural criterion to differentiate the interior point and the exterior point of any domain under an admissible meshfree discretization. This fact is reflected in the following proposition.

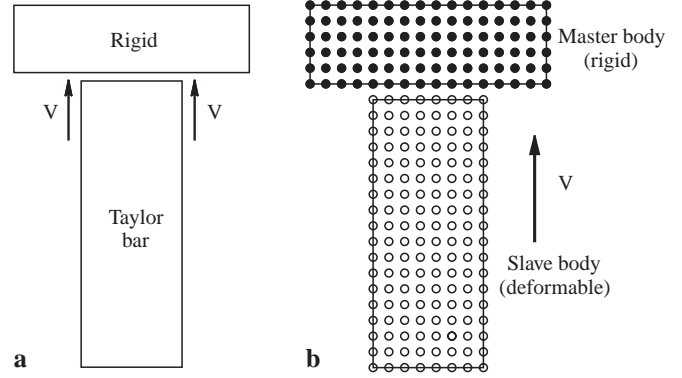


Fig. 14a-d. The collision and contact of deformable solid bar with rigid target: **a** problem statement; **b** admissible particle discretizations in different domain; **c** determinant of the moment matrix in master domain before penetration; **d** determinant of the moment matrix in master domain after penetration

Proposition 6.1 For a given admissible meshfree discretization in the effective domain $\Omega \in \mathbb{R}^n$, if a spatial point, X ($X \notin \Omega$), is sufficiently away from the effective domain Ω , the determinant of the moment matrix at point, $X : (X_1, X_2, X_3)$, will approach to zero; i.e. for given $\delta > 0$ $\exists \epsilon \geq 0$, such that if $\text{dist}\{\bar{\Omega}, X\} > \delta$

$$\det\{\mathbf{M}(X)\} < \epsilon, \quad X = (X_1, X_2, X_3) \quad (86)$$

The proof of the proposition will appear in [18]. This intrinsic property of moving least square based meshfree interpolant is illustrated in Fig 13(a) for one dimensional case and Fig 13b for two dimensional case.

Based on this property, one can easily check interpenetration of two different effective domains, as well as two distinct parts of one effective domain, which have admissible particle distribution, or discretization.

To illustrate the point, consider a simple Taylor bar impact problem, i.e. a deformable solid bar collides with rigid target as shown in Fig. 14a. Figure 14b shows two admissible particle distributions in rigid target (master body) and in deformable Taylor bar (slave body) respectively. By computing the determinant of the moment matrix in master domain for both master body and slave body (slave body is moving in the case), interpenetration of the two bodies can be easily detected. Figure 14(c) shows that before the Taylor bar collides with the rigid

target, the determinant of the slave body in master domain is either negative, or close to zero, whereas the master body itself has a almost constant value of determinant of moment matrix with respect to master domain particle distribution. After the penetration occurs, one can see from Fig. 14(d) that at the contact region the determinant of the moment matrix in slave body with respect to master domain particle distribution is on longer zero, and it has a finite, positive value. In computation, one can set a proper tolerance to signal the occurrence of the penetration. Again for a complete exposition, proofs and numerical examples, readers are referred to the incoming paper [18].

7

Concluding remarks

Previously, there have been a few studies using meshfree interpolants to solve thin plate, and Mindlin-Reissner plate problem (e.g. Donning and Liu [7]). The difference that distinguishes this study from the previous studies is that we use window based higher order meshfree interpolants to directly simulate large deformation of thin shell structures as a 3-D continuum. The numerical results shown here for three different constitutive models have demonstrated that the meshfree approach is viable in 3-D direct simulation of thin shell structures that are undergoing extremely large deformation.

The main advantage of using meshless methods in simulating thin shell structure is its remarkable simplicity. The best part of this approach is its capacity to compute extremely large deformation without any complication in both mechanics theory as well as finite element formulations, of course, further comparison studies should be conducted to quantitatively evaluate its numerical accuracy.

For all the computations done in this paper, a $2 \times 2 \times 2$ integration algorithm is adopted in each integration cell. Since the cubic spline window-based tri-linear shape function is at least C^4 in any specific direction, the integration scheme used here under-integrates the weak form, and hence it shall be regarded as a “reduced integration”. However, the good part of this scheme is one may not experienced any spurious modes due to such mild “reduced integration”, i.e. one may not observe rank deficiency caused by such under integration scheme in certain parameter range, which suggests that this scheme enable us to get rid of locking without even doing any hour-glass control at all. As one explanation offered at the beginning, we argued that since window based meshfree methods is a special “higher order manifold” discretization, the increase the smoothness of the meshfree shape function does not necessarily correspond to the increase of the total numbers of particles in discretization. Thus some “mild” reduced integration won’t cause rank deficiency. We would like also to point out that if 1-point integration is used, it will still cause spurious modes, but remarkably different from the finite element methods, as one keep increase the dilation parameter of the window function, or equivalently the support size of the shape function, such spurious modes may be suppressed automatically in meshfree computations without special hour-glass control. We would like to remark, in particular, that there is a

speculation that window function based meshfree interpolants may bypass some of the difficulties that lower order finite element methods are suffering, such as volumetric and shear locking, and hence bypass some special treatments or technologies designed for lower order finite elements.

At present moment, it appears to us that the major shortcoming of using 3-D meshfree formulation to compute thin shell structures is the restricted time step size used in the explicit computation. Nevertheless, we have successfully used only two layers of particles in thickness direction in computations, which are only deployed on the upper surface and the lower surface of the shell, the small time step problem is thus minimized to certain extent.

References

1. Atluri SN, Zhu T (1988) A new meshfree local Petrov-Galerkin(mlpg) approach in computational mechanics. *Comput. Mech.* 22:117-127
2. Atluri SN, Zhu T (1998) A new meshfree local Petrov-Galerkin(mlpg) approach to nonlinear problems in computer modeling and simulation. *Comp. Modeling and Simulation in Eng.* 3:187-196
3. Basar Y, Itskov M (1988) Finite element formulation of the ogden material model with application to rubber-like shells. *Int. J. Num. Meth. Eng.* 42:1279-1305
4. Belytschko T, Krongauz Y, Organ D, Fleming M, Krysl P (1996) Meshless methods: An overview and recent developments. *Comp. Meth. App. Mech. Eng.* 139:3-48
5. Chen JS, Pan C, Wu CT (1997) Reproducing kernel particle methods for rubber hyperelasticity *Comput. Mech.* 19:211-227
6. Chen JS, Pan C, Wu CT, Liu WK (1997) Reproducing kernel particle methods for large deformation analysis of nonlinear structures. *Comp. Meth. Appl. Mech. Eng.* 139:195-229
7. Donning B, Liu WK (1998) Meshless methods for shear-deformable beams and plates. *Comp. Meth. Appl. Mech. Eng.* 47-72
8. Fired I, Johnson AR (1988) A note on elastic energy density function for largely deformed compressible rubber solids. *Comp. Meth. Appl. Mech. Eng.* 53-64
9. Güther FC, Liu WK (1998) Implementation of boundary conditions for meshless methods. *Comp. Meth. Appl. Mech. Eng.* 163:205-230
10. Simo JC, Hughes TJR (1998) *Computational inelasticity*. Springer, New York
11. Hughes TJR (1984) Numerical implementation of constitutive models: Rate-independent deviatoric plasticity. In: S. Nemat-Nasser (ed.) *Theoretical Foundations for Large Scale Computations of Nonlinear Material Behavior*, pp 29-57. Martinus Nijhoff Publishers
12. Hughes TJR, Liu WK (1981) Nonlinear finite element analysis of shells: Part i. Three-dimensional shells. *Comp. Meth. App. Mech. Eng.* 26:331-362
13. Hughes TJR, Liu WK (1981) Nonlinear finite element analysis of shells: Part ii. Two-dimensional shells. *Comp. Meth. App. Mech. Eng.* 27:167-181
14. Li S, Liu WK, Hao W, Belytschko T (1999) Meshfree simulations of the propagation of dynamic shear band. Technical Report 99-04, Dept. of Mechanical Engineering, Northwestern University
15. Li S, Liu WK (1999) Numerical simulations of strain localization in inelastic solids using meshfree methods. Accepted for publication in: “*International Journal of Numerical Methods for Engineering*”
16. Li S, Liu WK (1999) Reproducing kernel hierarchical partition of unity Part i: Formulation & theory. *Int. J. Num. Meth. Eng.* 45:251-288

17. Li S, Liu WK (1999) Reproducing kernel hierarchical partition of unity Part ii: Applications. *Int. J. Num. Meth. Eng.* 45:251–288
18. Li S, Qian D, Liu WK, Belytschko T (1999) A meshfree impact-contact algorithm and its applications. Submitted to *Comp. Meth. Appl. Mech. Eng.*
19. Liu WK, Chen Y, Chang CT, Belytschko T (1996) Advances in multiple scale kernel particle methods. *Comput. Mech.* 18:73–111
20. Liu WK, Chen Y, Jun S, Chen JS, Belytschko T, Pan C, Uras RA, Chang CT (1996) Overview and applications of the reproducing kernel methods. *Archives of Computational methods in Engineering: State of the art review* 3:3–80
21. Liu WK, Guo Y, Tang S, Belytschko T (1998) A multiple-quadrature eight-node hexahedral finite element for large deformation elastoplastic analysis. *Comp. Meth. App. Mech. Eng.* 154:69–132
22. Liu WK, Hu YK, Belytschko T (1994) Multiple quadrature underintegrated finite elements. *Int. J. Num. Meth. Eng.* 37:3263–3290
23. Liu WK, Jun S, Zhang S (1995) Reproducing kernel particle methods. *Int. J. Num. Meth. Fluids* 20:1081–1106
24. Liu WK, Li S, Belytschko T (1997) Moving least square reproducing kernel method Part i: Methodology and convergence. *Comp. Meth. Appl. Mech. Eng.* 143:422–433
25. MacNeal RH, Harder RL (1985) A Proposed standard set of problems to test finite element accuracy. *Finite Element Analysis and Design*, 11:3–20
26. Needleman A (1988) Material rate dependent and mesh sensitivity in localization problems. *Comp. Meth. Appl. Mech. Eng.* 68–85
27. Pan J (1993) Perturbation analysis of shear strain localization in rate sensitive materials. *Int. J. Solids and Struct.* 19:153–164
28. Peirce D, Shih CF, Needleman A (1984) A tangent modulus method for rate dependent solids. *Comp. Struct.* 875–887
29. Shawki TG, Clifton RJ (1989) Shear band formation in thermal viscoplastic materials. *Mechanics of Materials*, 8:13–43
30. Simo JC, Rifai MS (1990) A Class of mixed assumed strain methods and the methods of incompatible modes. *Int. J. Num. Meth. Eng.* 29:1595–1638
31. Stanley GM (1985) Continuum-based shell elements. PhD thesis, Stanford University
32. Stolarski H, Belytschko T (1983) Shear and membrane locking in curved shell elements. *Comp. Meth. Appl. Mech. Eng.* 41:279–296
33. Zeng Q, Combescure A (1998) A new one-point quadrature general nonlinear quadrilateral shell element with physical stabilization. *Int. J. Num. Meth. Eng.* 42:1307–1338
34. Zhu T, Zhang J, Atluri SN (1998) A meshless local boundary integral equation (lbie) method for solving nonlinear problems. *Comput. Mech.* 22:174–186